Ultrasound in Med. & Biol., Vol. 33, No. 3, pp. 389–401, 2007

0301-5629/07/$–see front matter

ELSEVIER

doi:10.1016/j.ultrasmedbio.2006.07.037

● *Original Contribution*

ULTRASONIC CHARACTERIZATION OF WHOLE CELLS AND ISOLATED NUCLEI

LINDA R. TAGGART,*‡ RALPH E. BADDOUR,* ANOJA GILES,‡ GREGORY J. CZARNOTA,*†§¶ and MICHAEL C. KOLIOS*§

*Departments of Medical Biophysics and †Radiation Oncology, University of Toronto, Toronto, ON, Canada; ‡Ontario Cancer Institute/Princess Margaret Hospital, University Health Network, Toronto, ON, Canada; §Department of Physics, Ryerson University, Toronto, ON, Canada; and ¶Department of Radiation Oncology, Toronto Sunnybrook Regional Cancer Centre, Toronto, ON, Canada

(*Received* 17 *August* 2005; *revised* 22 *July* 2006; *in final form* 27 *July* 2006)

Abstract—High frequency ultrasound imaging (20 to 60 MHz) is increasingly being used in small animal imaging, molecular imaging and for the detection of structural changes during cell and tissue death. Ultrasonic tissue characterization techniques were used to measure the speed of sound, attenuation coefficient and integrated backscatter coefficient for (a) acute myeloid leukemia cells and corresponding isolated nuclei, (b) human epithelial kidney cells and corresponding isolated nuclei, (c) multinucleated human epithelial kidney cells and d) human breast cancer cells. The speed of sound for cells varied from 1522 to 1535 m/s, while values for nuclei were lower, ranging from 1493 to 1514 m/s. The attenuation coefficient slopes ranged from 0.0798 to 0.1073 dB mm^{-1} MHz^{-1} for cells and 0.0408 to 0.0530 dB mm^{-1} MHz^{-1} for nuclei. Integrated backscatter coefficient values for cells and isolated nuclei showed much greater variation and increased from 1.71×10^{-4} Sr^{-1} mm^{-1} for the smallest nuclei to 26.47×10^{-4} Sr^{-1} mm^{-1} for the cells with the largest nuclei. The findings suggest that integrated backscatter coefficient values, but not attenuation or speed of sound, are correlated with the size of the nuclei. (E-mail: mkolios@ryerson.ca) **© 2007 World Federation for Ultrasound in Medicine & Biology.**

Key Words: **High-frequency ultrasound, Ultrasonic tissue characterization, Isolated nuclei.**

INTRODUCTION

Ultrasound imaging is the most frequently used clinical imaging modality, accounting for almost 25% of all imaging procedures (Forsberg 2003). Recent advances in transducer technology and electronics have increased ultrasonic frequencies to 20 to 60 MHz, providing better image resolution at the expense of reduced ultrasound penetration depth (Foster et al. 2000). The associated ultrasound wavelengths are of the order of 25 to 75 μm, the same order of magnitude as the size of cells. Imaging cell ensembles results in a speckle pattern because, even at these high frequencies, individual cells cannot be resolved. Recent applications of high-frequency, ultrasound imaging (often referred to as ultrasound biomicroscopy) are in the fields of developmental and tumor biology (Foster et al. 2000), molecular imaging (Liang et al. 2003), ophthalmology (Pavlin et al. 1991), tumor characterization (Oelze et al. 2004) and monitoring anticancer treatment effects (Czarnota et al. 1999). Tissue scattering and attenuation at these frequencies are not well understood, necessitating ultrasonic characterization experiments.

Our group has shown that high-frequency ultrasound can detect changes in cell morphology during various forms of cell death (Czarnota et al. 2002; Kolios et al. 2002, 2003; Tunis et al. 2005). One such process is apoptosis, a significant process in normal prenatal development and potentially in the response of tumors to anticancer agents (Hengartner 2000). The most striking morphologic features of apoptosis are the condensation and fragmentation of the nucleus, as well as blebbing of the cell membrane (Hengartner 2000). We have shown that high-frequency ultrasound is sensitive to apoptosis *in vitro* and *in vivo* (Czarnota et al. 1999). Apoptotic cells and tissues can exhibit up to a sixteen-fold increase in backscatter intensity in comparison with viable cells, as well as subtle changes in the power spectrum. Moreover, similar changes in

Address correspondence to: Dr. Michael C. Kolios, Ryerson University, Department of Physics, 350 Victoria Street, Toronto, Ontario, Canada, M5B-2K3. http://www.physics.ryerson.ca E-mail: mkolios@ryerson.ca

ultrasound backscatter have been detected in cells (Kolios et al. 2003) and tissues (Vlad et al. 2005) exposed to lethal ischemic insults. These backscatter changes are not well understood because the nature of the interaction between high-frequency ultrasound waves and cellular or nuclear scatterers is not yet fully known. Many studies have been performed on ultrasonic tissue characterization at lower frequencies (for a review see Shung and Thieme 1993) and recent work has been done at higher frequencies for tissue such as skin (Raju and Srinivasan 2001), eye (Ursea et al. 1998) and blood (Cloutier et al. 2004; Lupotti et al. 2004). Work using tumors and cell systems has shown the potential for tissue characterization, especially at higher frequencies (Kolios et al. 2002, 2004; Oelze et al. 2004; Tunis et al. 2004). An examination of ultrasonic parameters from cells with different sizes and different properties may yield valuable insights into the backscattering process.

In this study, we ultrasonically characterized various types of cells and their isolated nuclei that differ in size and, most likely, mechanical properties. Measurement of the speed of sound, attenuation and integrated backscatter coefficient of these samples provides information regarding the physical characteristics of the cells and the nature of the scatterers. These results may also play an important role in the development of quantitative models of the scattering process (Baddour et al. 2005), which in turn could be utilized to generate parametric images of diagnostic relevance to clinicians and also could aid in the design of appropriate pulsing sequences to enhance tissue contrast.

METHODS

Cell preparation

Acute myeloid leukemia cells (OCI-AML-5) (Wang et al. 1991) were the first cell type used. Cells obtained from frozen stock samples were cultured at 37°C in 150 mL of α minimum essential medium (Invitrogen Canada Inc., Burlington, Ontario, Canada) and antibiotics (100 mg/L streptomycin (Bioshop, Burlington, Ontario, Canada), 100 mg/L penicillin (Novapharm Biotech Inc., Toronto, Ontario, Canada) with 5% fetal bovine serum (Cansera International Inc., Etobicoke, Ontario, Canada). OCI-AML-5 cells with a short time in culture (3 to 4 months) as well as a longer time in culture (>1 y) were used as the size of the cells increased and the phenotype changed with longer culture times due to natural differentiation. Cells were harvested by centrifugation at a centripetal force of 960 *g* for 6 min at 4°C. Minimum essential medium (MEM) was aspirated and cells washed in phosphate-buffered saline (PBS; in distilled water: 8 g/L sodium chloride, 0.2 g/L potassium chloride, 0.132 g/L calcium chloride, 0.10 g/L magnesium chloride, 1.15 g/L sodium phosphate, 0.2 g/L potassium phosphate) and centrifuged again at 2000 *g* for 10 min at 4°C.

Nuclear isolations were performed using a detergent method similar to that of Muramatsu and colleagues (Muramatsu et al. 1974, 1977). OCI-AML-5 cells to be used for the nuclear isolation were washed in PBS and centrifuged at 2000 *g* for 10 min at 4°C. Cells underwent hypotonic shock by adding 20 volumes of a reticulocyte standard buffer (RSB) consisting of 0.01 M trizma base, 0.01 M NaCl and 1.5 mM $MgCl\text{-}6H_20$ (Sigma-Aldrich Canada Ltd., Oakville, Ontario, Canada) with protease inhibitors (one complete mini, EDTA-free protease inhibitor cocktail tablet (Roche Diagnostics, Laval, Quebec, Canada) for each 10 mL of RSB) added immediately before use. The suspension of cells in RSB was left to stand in an ice bath for 10 min, then centrifuged at 500 *g* for 5 min at 4°C. Swollen cells were then resuspended in the same volume of RSB as employed in the first hypotonic shock procedure. Nonidet P40 (Roche Diagnostics, Laval, Quebec, Canada) was added to a final concentration of 0.02% from a freshly prepared 10% stock solution. When nuclei were visible under the microscope, the solution was centrifuged at 500 *g* for 5 min at 4°C. Nuclei were washed twice in PBS containing divalent cations at 500 *g* for 5 min at 4°C.

Human epithelial kidney cells (HEK-293) were the second cell type used. These were selected because they are larger than OCI-AML-5 cells and upon chemical intervention provide a multinucleated cell phenotype (Jin and Woodgett 2005). This structural phenotype is of interest because of the hypothesis that the nucleus contributes to the ultrasound backscatter (Czarnota et al. 1997). The cells were cultured at 37°C in 17 mL of Dulbecco's media H21 (Invitrogen Canada Inc.) plus antibiotics, 10% fetal bovine serum (FBS) and 150 μg/mL geneticin (Hoffmann-La Roche Ltd., Canada). Cells were washed with PBS, harvested by trypsinization and centrifuged at 100 *g* for 5 min, then washed with PBS and centrifuged at 100 *g* for 5 min. For nuclear isolation, HEK cells underwent a wash in PBS without divalent cations and were centrifuged at 500 *g* for 5 min at 4°C. Nuclei were prepared as above, except that the necessary concentration of Nonidet P40 was 0.06%. Nuclei were centrifuged at 500 *g* for 5 min, washed twice with PBS containing divalent cations and centrifuged at 700 *g* for 5 min.

Large multinucleated HEK cells were produced by exposing HEK-293 cells to 4-hydroxytamoxifen at a concentration of 1 μM. After at least 10 days, cells were washed with PBS, harvested by trypsinization and centrifugation at 100 *g* for 5 min. Cells were then washed in PBS and centrifuged again for an additional 5 min.

Finally, to investigate another cell line with similar

size to the HEK cells but possibly with different mechanical properties, human breast cancer cells (MT-1 Luc$^+$) were used. The cells were cultured at 37°C in 17 mL of MEM F15 medium (Invitrogen Canada Inc.) plus antibiotics, 1 mM pyruvate and 1.5 g/L bicarbonate with 10% FBS. For this cell line, the nucleus-isolation procedure described above was not successful in extracting a consistent phenotype of nucleus and therefore only intact cells were examined.

Before ultrasound data acquisition, all samples consisting of cells or nuclei were prepared by centrifugation in a custom-built sample holder, described below. Upon completion of ultrasound imaging, a sample of cells or nuclei from the pellet was resuspended in PBS, placed on a glass slide and covered with a slide cover. No fixation or staining was done. Light microscopy was performed at 40× objective magnification and cell diameters were measured using a reticule. The remainder of each pellet was fixed in 2% glutaraldehyde for further ultrastructural analysis using electron microscopy.

Data acquisition

A VisualSonics VS40B high-frequency ultrasound device (VisualSonics Inc., Toronto, Ontario, Canada) was used to image all samples. A 40-MHz f/2 transducer was used for the experiments. The transducer had a diameter of 6 mm, a radius of curvature of 6 mm and a −3 dB bandwidth of approximately 40 MHz. The experimental set-up is shown in Figure 1. A sample holder was constructed using a flat polished fused silica crystal (Edmund Industrial Optics Inc., Barrington, NJ, USA, part 43424) base glued to a stainless steel disk (Fig. 1a). Both the base and the disk were 2.54 cm in diameter. Two cylindrical holes cut through the stainless steel disk created wells 5 mm in diameter and 2.99 mm deep. Cells or isolated nuclei were prepared by centrifugation in one well and the other well served as a calibration reference. The sample holder was placed in a 6.8 cm diameter polyethylene container (weight boat) containing PBS. The solution acted as a coupling medium and also as the reference material in the well that did not containing the sample.

Three sets of data were collected, each at room temperature (20°C). The region-of-interest (ROI) for the pellet was obtained by selecting the region with the most uniform pellet thickness from B-scan images. The ROI for the reference well was selected to be the same size as that of the pellet well and centered in the reference well. Raw radio-frequency (RF) data were acquired at a sampling frequency of 500 MHz in a raster scan at a minimum of 90 independent locations in each well. Ten A-scans collected at each location were averaged, to reduce noise.

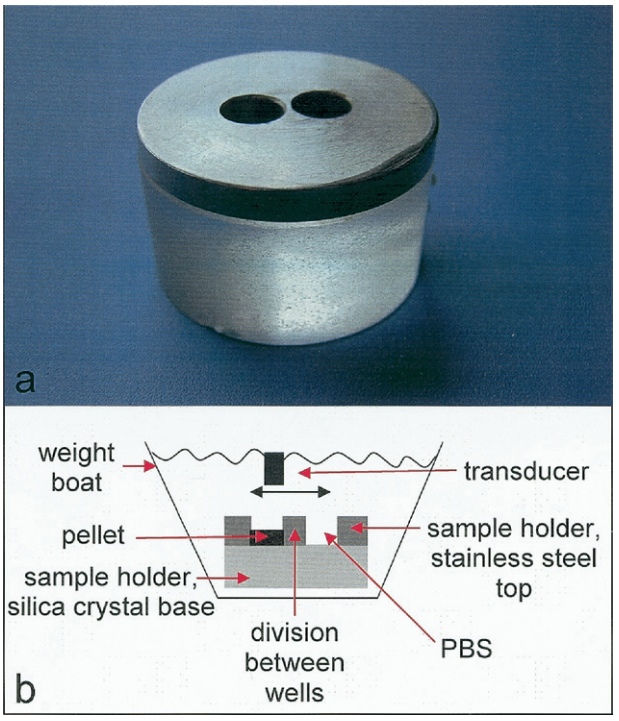

Fig. 1. (a) Photograph of sample holder consisting of a silica crystal base and a stainless steel top. (b) Schematic of experimental set-up for measurement of ultrasonic properties. A stainless steel top was glued onto a silica crystal, forming a well in which cells were pelleted and an empty well for the reference coupling medium. The apparatus was situated in a weight boat containing PBS for the experiments.

The position of the transducer focus with respect to the holder was optimized for the type of ultrasonic data collected. The first sets of acquisitions were performed to calculate the speed of sound. With the transducer focus placed at the center of the wells, data were acquired at two different levels of amplifier gain; a lower gain was used to avoid saturating the acquisition electronics due to the reflection from the base of the well and a higher gain to fully utilize the 8-bit dynamic range of the acquisition electronics when measuring signals from the cell pellet. Additional A-scans were obtained from the divider between the wells (see Fig. 1), at a low and a high gain. In the attenuation calculation experiments, the transducer focus was aligned with the well base. A-scans were collected from each of the wells with the amplifier gain adjusted to maximize the amplitude of the well reflections without saturating the acquisition electronics. For the backscatter data, the transducer was focused at the pellet center. A-scans were collected from the pellet-containing well. A-scans were also collected from 14 locations on a calibration target: this was a flat polished fused silica crystal (Edmund Industrial Optics Inc., USA,

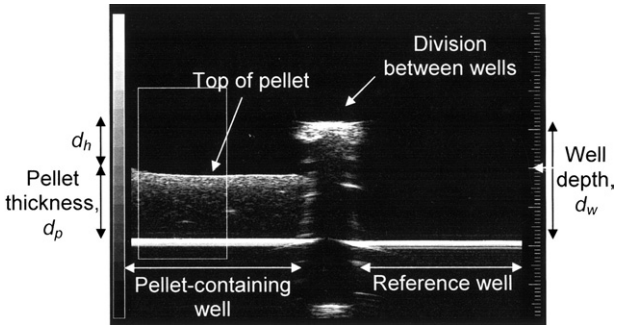

Fig. 2. Ultrasonic image of the sample holder with an AML pellet in the left well, and the coupling medium in the right well. The image size is 8 × 8 mm and the large divisions to the right are 1 mm. The triangle on the grid to the far right denotes the transducer focus, located at the center of the wells in this experiment. The slight elevation of the well bottom in the pellet-containing well compared with the reference well is due to the higher speed of sound in the sample.

part 43424). The transducer focus was aligned to the silica crystal/distilled water interface.

Data analysis

All signal analysis was performed using MATLAB (The Mathworks Inc., Natich, MA, USA). The acquired A-scans were used to calculate (a) the speed of sound, (b) the attenuation and (c) the integrated backscatter of the cell pellet.

Speed of sound

A relative time-of-flight method was employed to avoid directly measuring the thickness of the pellet, which would be difficult, given the small pellet height (~1.5 mm) and its location inside a stainless steel well. The average speed of sound was calculated:

$$\frac{1}{c_p} = \frac{1}{c_r} - \frac{\Delta t}{2d_p} \tag{1}$$

where c_p is the speed of sound in the pellet, c_r is the speed of sound in the PBS, d_p is the thickness of the pellet and Δt is the time difference between the arrival time of the echo from the base of the pellet-containing well and that from the base of the well containing the reference/coupling material. In Fig. 2, the different regions of the sample holder are depicted on a B-scan image. The reference speed of sound, c_r, was calculated using $2d_w/t_w$, where d_w is the well depth and t_w is the time difference in the mean arrival time of the reflection from the top of the division between the wells and that from the base of the reference well. Time of arrival was obtained by taking the Hilbert transform of the A-scan, finding the sample number corresponding to the maximum and calculating the corresponding time. This method was necessary because the reflection from the base of the pellet-containing well was preceded by the signal from the pellet, making it difficult to locate the first zero-crossing after the signal was detectable above noise. Δt was determined using the same definition for time of arrival.

To determine the pellet thickness d_p, the thickness of the PBS layer in the pellet-containing well (d_h in Fig. 2) was determined and then subtracted from the known well depth, d_w. Parameter d_h was calculated as $c_r t_h/2$, where t_h is the difference in the mean times of arrival of reflections from the top of the division between the wells and the top of the pellet. The time of arrival of the signal was determined by finding the first zero crossing after the signal emerged from the noise range.

Attenuation

A broadband technique was used to obtain the attenuation coefficient, $\alpha(\nu)$, as a function of frequency, ν, within the 6 dB bandwidth of the system. The calculation was performed as follows (D'Astous and Foster 1986):

$$\alpha(\nu) = \alpha_r(\nu) + \frac{20}{2d_z}\log_{10}\left(\frac{S_r(\nu)}{S_p(\nu)}\right) \tag{2}$$

where $\alpha_r(\nu)$ is the frequency-dependent attenuation of the PBS, which was taken to be similar to water, 2.1715×10^{-4} dB mm^{-1} MHz^{-2} at 20°C (Duck, 1990). At the frequency of 40 MHz used for this study, the contribution of $\alpha_r(\nu)$ is not negligible. $S_r(\nu)$ is the mean amplitude spectrum for the backscatter from the reference well, obtained by averaging the magnitude of the 2048-point fast Fourier transforms (FFTs) of all the well reflections. $S_P(\nu)$ is the mean amplitude spectrum for one location in the pellet-containing well, obtained by averaging all 10 of the echoes from that location in the frequency domain. Figure 3a shows a plot of the mean amplitude spectrum from the reference well and an overlay of the mean amplitude spectra for 30 locations in the pellet well. The thickness of the pellet, d_z, measured during the speed of sound calculation was used. The frequency-dependent attenuation coefficient was found for each location in the pellet. These values were then corrected for the PBS attenuation $\alpha_r(\nu)$ by converting the attenuation of water to a value at each discrete frequency with a corresponding attenuation. The attenuation of water was added to the attenuation of the pellet for each frequency to obtain $\alpha(\nu)$, as shown in Fig. 3b. Linear fits were found for each location in the pellet by linear least-squares regression analysis over the frequency range of 20 to 60 MHz. The mean and standard deviation of the spectral slope were found for each pellet, and the means for all pellets of one sample type were used to find a mean and standard deviation for each sample type.

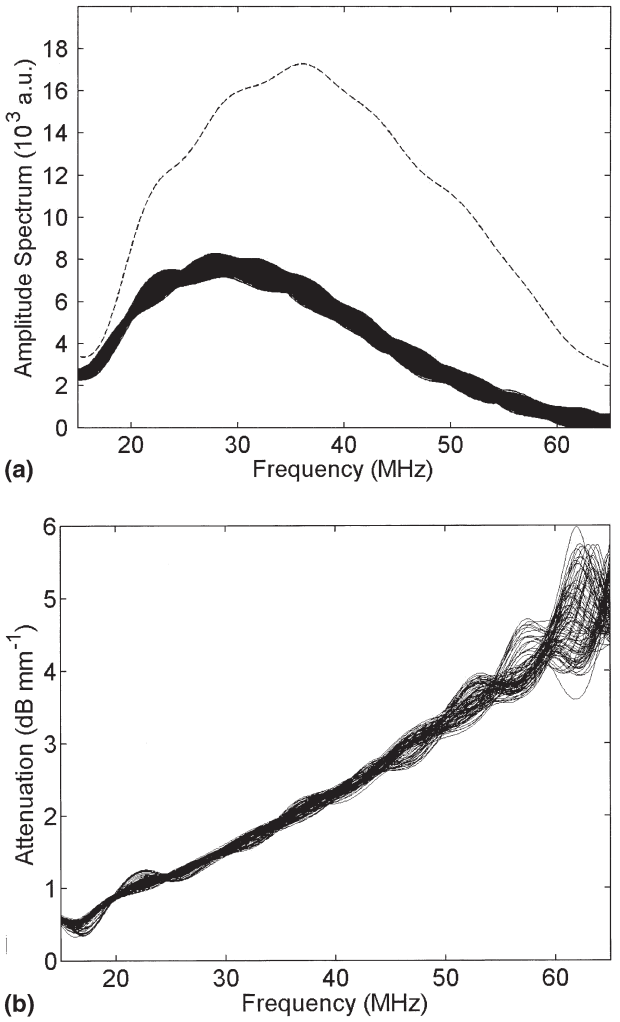

Fig. 3. Attenuation measurements (a) Plot of the mean amplitude spectrum from the reference well (dotted line) and an overlay of 30 scan lines of the mean amplitude spectra for different locations in the pellet well containing HEK cells. (b) Plot of $\alpha(\nu)$, in dB mm^{-1}, corrected for water attenuation. The frequencies used in the analysis were from 20 to 60 MHz, corresponding to the relevant transducer bandwidth.

Backscatter

To calculate the integrated backscatter, the frequency-dependent backscatter coefficient was first calculated. The backscatter coefficient was given by (Turnbull et al. 1989):

$$\mu(\nu) = \frac{1}{n}\sum_{i=1}^{n} \frac{R}{2\pi(1-\cos\theta)} \cdot \frac{\left|S_{pellet}(\nu)x10^{\frac{D\alpha(\nu)}{20}}\right|^2}{\left|S_{ref}(\nu)\right|^2} \cdot \frac{1}{\Delta z} \tag{3}$$

where $S_{pellet}(\nu)$ is the amplitude spectrum at one location in the pellet. It was calculated by averaging all of the magnitudes of the FFTs for the backscatter reflections at each location in the raster scan. To obtain $S_{pellet}(\nu)$, a time gate corresponding to half of the transducer depth of field was used. The speed of sound from that pellet was used to convert the half depth of field to a total time interval and, thus, the sample number corresponding to the start and end of the time gate could be found. D is the average distance traveled by the ultrasound signals within the time gate. The amplitude spectrum for each location was corrected by the factor $10^{\frac{D\alpha(\nu)}{20}}$ to compensate for the average frequency-dependent attenuation of the pellet (Worthington and Sherar 2001). The parameter $\alpha(\nu)$ is the frequency-dependent attenuation of the sample, as found in the attenuation analysis. $S_{ref}(\nu)$ is the amplitude spectrum taken from an average of the mag-

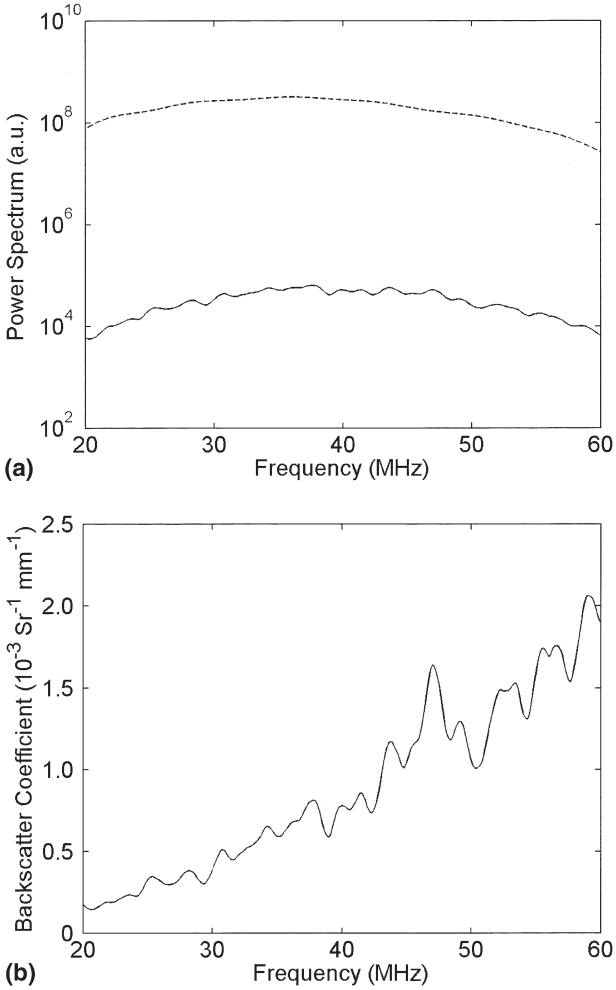

Fig. 4. Backscatter measurements (a) Plot of the mean power spectrum from the reference well (dotted line) and the ROI of the HEK cell pellet (solid). (b) Calculated backscatter coefficient as a function of frequency. The frequencies used in the analysis were from 20 to 60 MHz, corresponding to the relevant transducer bandwidth.

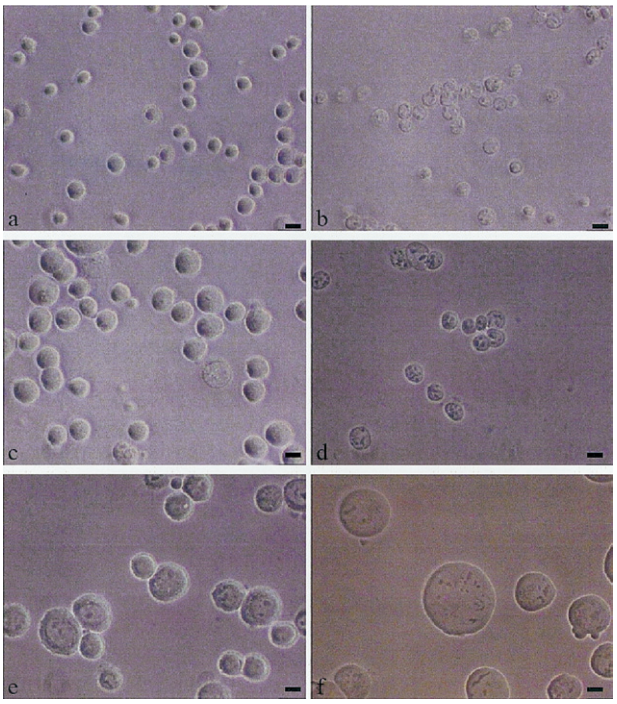

Fig. 5. Optical microscopy of (a) Whole OCI-AML-5 cells (short culture), (b) Isolated OCI-AML-5 nuclei (short culture), (c) Whole HEK cells, (d) Isolated HEK nuclei, (e) Whole MT1 cells and (f) Treated HEK cells. The scale bar, identical in all images, is 10 μm.

nitude of the FFTs of all reflections from the silica crystal reference in distilled water. This consisted of 140 A-scans in total, 10 at each of 14 positions. Figure 4a shows the mean power spectrum from the silica crystal reference and the mean power spectrum for one pellet, without the attenuation correction.

R is the intensity reflectance coefficient of the calibration interface (distilled water/silica crystal). It was calculated from:

$$R = \left(\frac{Z_2 - Z_1}{Z_2 + Z_1}\right)^2 \quad (4)$$

which holds when the angles of incidence and refraction are both equal to zero degrees. Z_1 and Z_2 are the acoustic impedances at 20°C of distilled water (1.482×10^5 g $s^{-1}cm^{-2}$) (Duck 1990) and silica crystal (12.584×10^5 g s^{-1} cm^{-2}, Edmund Industrial Optics Inc., USA), respectively. This yields an intensity reflectance coefficient (R) of 0.623. θ is the half angle subtended by the transducer at its focus and is equal to $\tan^{-1}$ (3/6), since the transducer radius is 3 mm and the focal length is 6 mm. The thickness of the pellet analyzed, Δz, corresponded to the time gate, which was equal to half the depth of field. Backscatter coefficients were determined in the frequency range of 20 to 60 MHz in steps of 0.12 MHz. Figure 4b shows the mean frequency-dependent backscatter coefficient for a single pellet. The integrated backscatter coefficient at each location was then calculated numerically, according to Raju and Srinivasan (2001):

Integrated backscatter coefficient =

$$\frac{1}{40\ \text{MHz}} \int_{20\ \text{MHz}}^{60\ \text{MHz}} \mu(v)dv \quad (5)$$

where $\mu(v)$ is the frequency-dependent backscatter coefficient. The mean integrated backscatter and standard deviation between different locations were calculated for each pellet. The mean and standard deviation between pellets were calculated for each sample type.

RESULTS

Eight different sample types were ultrasonically characterized, consisting of either intact cells, isolated nuclei or, in the case of the HEK cells, transformed multinucleated cells. Light-microscope images of these samples are shown in Fig. 5. The isolated nuclei (Fig. 5b and d) appear to retain their shape and integrity. Significant differences in cell or nucleus diameter were measured between samples. Average diameters and standard deviations are shown in Table 1. Values were based on measurement of 10 to 35 diameters, with the higher sample sizes for cells that were more variable in size. Ultrastructural features of typical cells and isolated nuclei are shown in Fig. 6. Again, the nucleus structural phenotype is similar between the isolated and *in situ* nuclei. Furthermore, Fig. 6f clearly shows the multinucleated phenotype of the treated HEK cells.

Table 2 shows the calculated speed of sound for the various types of whole cells and isolated nuclei. Average values for the speed were obtained by repeating each measurement on two or three different pellets prepared independently from different sets of cells. Speed of

Table 1. Average diameter of cells and nuclei

Sample type	Average diameter (μm)	Standard deviation (μm)
OCI-AML-5 cells - short culture	9.3	1.0
OCI-AML-5 cells - long culture	12.0	2.3
OCI-AML-5 nuclei - short culture	9.1	1.4
OCI-AML-5 nuclei - long culture	11.5	2.6
HEK cells	18.4	3.7
HEK nuclei	12.5	2.4
Multinucleated HEK cells	33.8	16.8
MT-1 cells	20.1	3.7

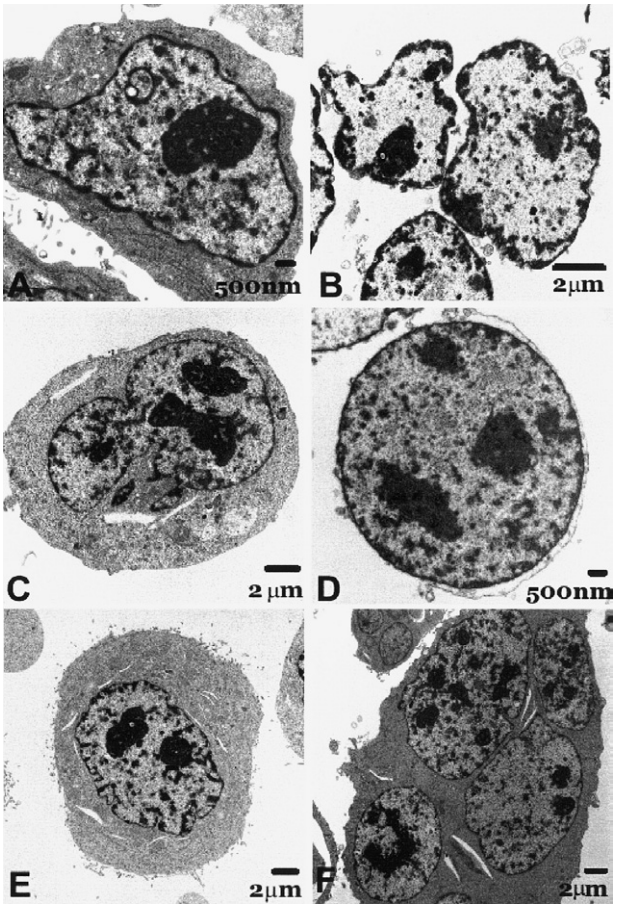

Fig. 6. Electron microscopy of (a) Whole AML cells, (b) Isolated AML nuclei, (c) Whole HEK cells, (d) Isolated HEK nuclei, (e) Whole MT1 cells and (f) Treated HEK cells. The scale bar varies from image to image. The images represent cross-sections through the cells. The multinucleated phenotype of the treated HEK cell is apparent in (f).

sound for cells was higher than the speed of sound for nuclei in all cases.

The mean and standard deviation of the spectral attenuation slope for each sample type can be found in Table 3. Values with and without the correction for the attenuation of PBS are shown. The correction caused all magnitudes to increase, but general trends did not change. For isolated nuclei, the attenuation slope values were approximately half that of whole cells, which ranged from 0.0798 to 0.1073 dB mm^{-1} MHz^{-1}.

Table 4 shows the average integrated backscatter coefficient and standard deviation for each sample type. Backscatter increased with frequency for all pellets. The B-scan images were consistent with these differences in backscatter. Figure 7 shows ultrasound images from two different cell pellets, one formed from OCI-AML-5 cells and the other, from MT-1 cells. The MT-1 cell pellet backscatter intensity is approximately 15 times greater than the OCI-AML-5 cell pellet. To investigate the relationships of these data to cell or nucleus size, Figs. 8, 9 and 10 plot the data as a function of cell or nuclear diameter.

DISCUSSION

A broadband 40MHz transducer was used to characterize cells ultrasonically and, when possible, their corresponding isolated nuclei. After the nuclear isolation procedure, the structural phenotype of the nucleus was similar to that seen for the nucleus *in situ*. Speed of sound, attenuation and integrated backscatter were calculated for several cell lines of different size and, likely, mechanical properties.

The speed of sound is higher in cells than in isolated nuclei for all cases (Table 2). Values for intact cells range from 1522 to 1535 m/s, while those for nuclei range from 1493 to 1514 m/s. The isolated nuclei appear to have an overall lower speed of sound than cells, irrespective of size (Fig. 8). For example, long culture OCI-AML-5 cells and HEK nuclei were of almost the same diameter, however, the HEK nuclei had a lower speed of sound. The lower speed of sound measured in the isolated nuclei was somewhat unexpected, as one would expect nuclei, with a higher average density (Meselson and Stahl 1958), to have a higher speed of sound. The nucleus compressibility, however, is not known and, without cytoplasmic support, compressibility may be altered by the procedure of nuclear isolation.

To our knowledge, no other studies have discussed the speed of sound of cell ensembles specifically. Most previous studies have examined bulk tissue properties as a whole. For example, Saijo et al. (1997) obtained a sound speed of 1620 m/s in normal human myocardium. Values for other human soft tissues include 1532 to 1537 m/s for human brain at 22°C, 1527 m/s for human eye (choroid) at 20°C, 1459 to 1487 m/s for fat at 24°C and 1575 m/s for spleen at 23 to 26°C (Duck 1990). Therefore, the values obtained in this study are within the range of other soft tissues.

Table 2. Average speed of sound and standard deviation for various pellets

Sample type	Average speed (m/s)	Standard deviation (m/s)
OCI-AML-5 cells - short culture	1535	6
OCI-AML-5 cells - long culture	1529	10
OCI-AML-5 nuclei - short culture	1503	6
OCI-AML-5 nuclei - long culture	1514	6
HEK cells	1523	9
HEK nuclei	1493	4
Multinucleated HEK cells	1522	3
MT-1 cells	1527	7

Table 3. Average spectral slope of the attenuation coefficient and standard deviation for various pellets. Values before and after correction for the attenuation of PBS are shown

Sample type	Slope (corrected) (dB mm^{-1} MHz^{-1})	Standard dev (corrected) (dB mm^{-1} MHz^{-1})	Slope (uncorrected) (dB mm^{-1} MHz^{-1})	Standard dev (uncorrected) (dB mm^{-1} MHz^{-1})
OCI-AML-5 cells - short culture	0.0805	0.0042	0.0631	0.0039
OCI-AML-5 cells - long culture	0.0867	0.0037	0.0680	0.0068
OCI-AML-5 nuclei - short culture	0.0466	0.0077	0.0289	0.0081
OCI-AML-5 nuclei - long culture	0.0530	0.0175	0.0354	0.0178
HEK cells	0.0830	0.0085	0.0653	0.0081
HEK nuclei	0.0408	0.0026	0.0235	0.0027
Multinucleated HEK cells	0.0798	0.0003	0.0626	0.0003
MT-1 cells	0.1073	0.0007	0.0902	0.0006

Attenuation measurements also revealed a significant difference between whole cells and their isolated nuclei. The average attenuation coefficient slopes for whole cells range from 0.0798 to 0.1073 dB mm^{-1} MHz^{-1}, while values for nuclei ranged from 0.0408 to 0.0530 dB mm^{-1} MHz^{-1}. No significant association appeared to exist between cell size and attenuation (Fig. 9). For example, as shown in Table 1, only a very small size difference exists between short or long-culture OCI-AML-5 cells and their respective isolated nuclei (the nuclear-to-cell diameter ratio is high); however, the spectral attenuation slope of the cells is almost twice that of the nuclei in both cases. The HEK cells, which have a smaller ratio of nuclear diameter to cell diameter, also had a spectral attenuation slope approximately twice that of the HEK nuclei. Figure 9 demonstrates that attenuation slope data were clustered in two categories, those of whole cells and those of isolated nuclei. Ultrasonic attenuation is due to losses from absorption and scattering, with absorption contributing to most of the energy loss (Bamber 2004). The fact that the backscatter is greater for the larger cells (Tables 1 and 4) suggests that, even at these high frequencies, absorption contributes to most of the ultrasonic energy loss. At physiological pH levels, perturbation of the hydration layers around macromolecules is likely to be responsible for the most important relaxation mechanisms (Sarvazyan and Hill 2004). Consequently, the macromolecules responsible for this absorption possibly may prove to be abundant outside the nucleus, which would cause attenuation in whole cells. This is a likely situation, because cell mechanical properties may be determined largely by the underlying cytoskeleton (Costa 2003). A large body of work recently has been produced examining the mechanical properties of cells. For example, Tseng et al. (2004) showed that the nucleus is elastic at high rates of deformation (as in ultrasound imaging) and more liquid-like at low rates of deformation and that the viscoelastic modulus of the nucleus is at least two times greater than that of the cytoplasm), which suggests that the nucleus is a scattering source candidate, previously hypothesized by the authors (Kolios et al. 2003).

To our knowledge, this is the first ultrasonic attenuation measurement on samples of cells. However, several other studies have measured this parameter in tissues at high frequencies. For example, Raju and Srinivasan (2001) found that the attenuation slope for *in vivo* human forearm dermis ranged from 0.08 to 0.39 dB mm^{-1} MHz^{-1} when measured with three transducers with center frequencies ranging from 28 to 44 MHz. Rat hearts were found to have an attenuation slope ranging from 0.15 to 0.17 dB mm^{-1} MHz^{-1} when measured at 40 MHz in a myocardial edema study (Dent et al. 2000). Human aorta had an attenuation slope of 0.19 to 0.36 dB

Table 4. Average integrated backscatter coefficient and standard deviation for various pellets. The last column shows the increase in backscatter of whole cells compared to the short culture OCI-AML-5 cells

Sample type	Integrated backscatter coefficient (IBC) (10^{-4} Sr^{-1} mm^{-1})	Standard dev (10^{-4} Sr^{-1} mm^{-1})	Factor increase in IBC compared to short culture AML cells
OCI-AML-5 cells - short culture	1.76	0.62	1
OCI-AML-5 cells - long culture	4.48	0.83	2.5
OCI-AML-5 nuclei - short culture	1.71	0.65	
OCI-AML-5 nuclei - long culture	4.30	3.18	
HEK cells	8.61	2.89	4.9
HEK nuclei	2.52	0.01	
Multinucleated HEK cells	8.61	2.24	4.9
MT-1 cells	26.47	6.71	15.0

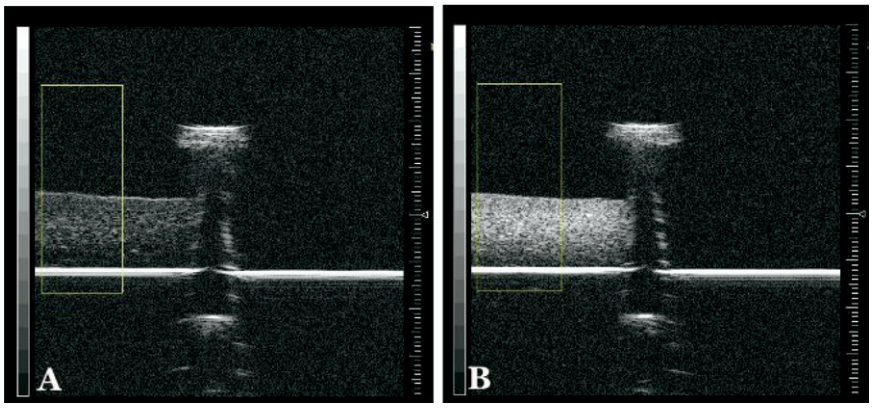

Fig. 7. Ultrasonic images from an (a) Short culture AML and (b) MT-1 cell pellet, acquired using identical gains. The rectangles outline the region from which the RF data were collected for this experiment. The MT-1 cell pellet has an integrated backscatter coefficient 15 times greater than that for the AML cells.

mm^{-1} MHz^{-1} when measured between 25 and 56 MHz (Bridal et al. 1997) and rat myocardium ranged from 0.123 to 0.226 dB mm^{-1} MHz^{-1}, depending on the age of the animal (Nguyen et al. 2001). Our values ranging from 0.0798 to 0.1073 dB mm^{-1} MHz^{-1} for cells and 0.0408 to 0.0530 dB mm^{-1} MHz^{-1} for nuclei are less than or equal to these reported values. Studies have shown that attenuation is correlated with collagen concentration (Nguyen et al. 2001). This may explain why these pure cell pellets have a lower attenuation than tissues, which presumably contain more collagen, due to their extracellular components.

Values of integrated backscatter coefficient are correlated with cell size, or, more specifically, nuclear size. For example, short-culture OCI-AML-5 cells and isolated nuclei were similar in size and had similar values of integrated backscatter coefficient (Table 4). The same was true of long-culture OCI-AML-5 cells and their isolated nuclei. Making comparisons between cell types, the correlation of integrated backscatter coefficient with size was even more apparent. For example, the only notable physical difference between the two types of OCI-AML-5 cells is that cells cultured for over 1 y had a diameter that was approximately 3 μm greater than those cultured for a few months. The backscatter was approximately 2.5 times greater in the larger long-culture OCI-AML-5 cells than it was in short-culture OCI-AML-5 cells (Table 4). This finding implies that the size of the dominant scattering source in cell pellets is proportional to cell size, although the available data do not provide a way of determining whether the principal scatterer is the cell itself, the nucleus or another cell component.

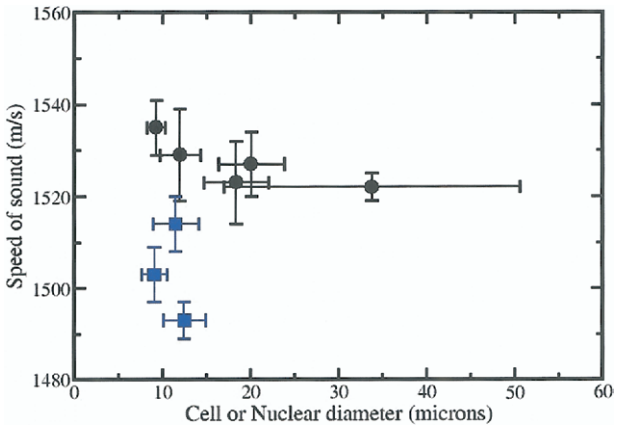

Fig. 8. Speed of sound plotted versus cell or nuclear diameter. The cell data are denoted by circles and the isolated nuclei, by the lighter colored squares. The large error bars of the 34 μm data point are for the multinucleated HEK cells.

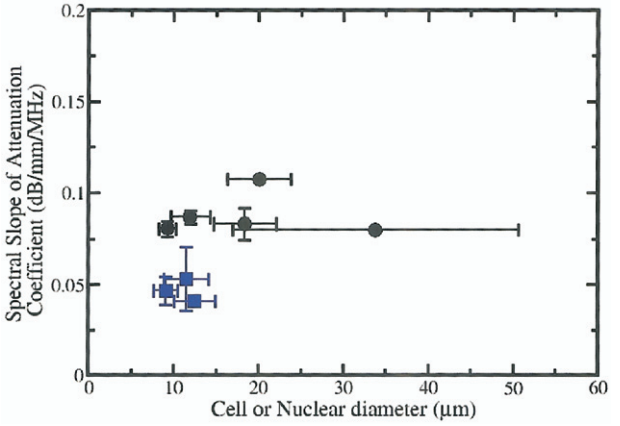

Fig. 9. Attenuation slope plotted versus cell or nuclear diameter. The cell data are denoted by circles and the isolated nuclei, by the lighter colored squares. Error bars are present on all data points but, in some cases, are too small to visualize. No correlation of cell size with slope is apparent, but the data are clustered between nuclei and whole cells.

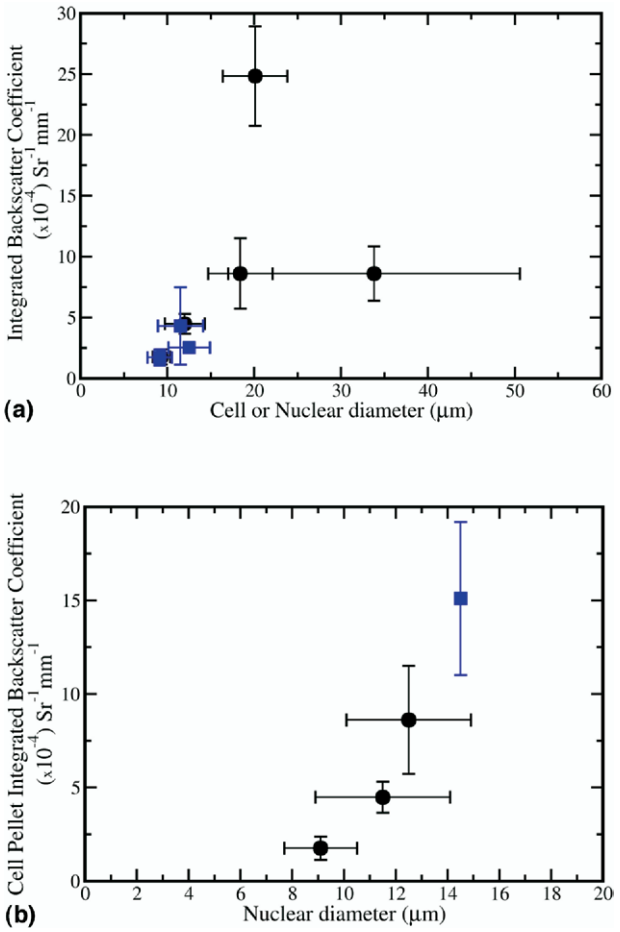

Fig. 10. Pellet integrated backscatter coefficient plotted versus (a) Cell or nuclear diameter and (b) Nuclear diameter. In (a), the cell data are denoted by circles and the isolated nuclei, by the lighter colored squares. In (b), the data were acquired from whole cells, with the diameter of the cell nucleus plotted along the x-axis. The square denotes the MT-1 cell line for which the nuclear diameter was measured by visual inspection of the microscopy images of whole cells.

Figure 10 shows the relationship between integrated backscatter and cell or nuclear diameter. The integrated backscatter increases with diameter. However, whereas the MT-1 cells had the highest value of integrated backscatter coefficient, the multinucleated-HEK cells, which were significantly larger on average, had a smaller coefficient value. HEK-293 cells treated with 4-hydroxytamoxifen increased considerably in size (Table 1) and contained multiple nuclei (Fig. 6f). They were included in this study to investigate the ultrasonic properties of large, multinucleated cells. The treatment results in cells of various sizes, containing a variable number of nuclei. This large variability is reflected in the standard deviation associated with the cell diameter of 33.8 ± 16.8 μm. The nonuniformity in the size of these cells and the number of nuclei must be taken into account when interpreting the data. Nonetheless, the fact that the multinucleated HEK cells had similar values of integrated backscatter coefficient compared with the nontreated HEK cells is surprising, even although their diameters varied on average by a factor of 1.8.

One possible interpretation of the data are that the size of the nucleus, not the size of the cell itself, dominates the backscatter in cell ensembles. These results are consistent with the nuclei being the dominant scatterers, because their sizes are similar for both HEK cell phenotypes. HEK cells and multinucleated HEK cells had an almost identical speed of sound, spectral attenuation slope and integrated backscatter. Moreover, HEK cells and the MT-1 cells have similar cell diameters, yet their integrated backscatter coefficient differs by a factor of three. Although we were not able to successfully isolate structurally intact nuclei from the MT-1 cells, visual inspection of the light microscopy (Fig. 5) indicates that MT-1 cells have a large nucleus, with a diameter of 15.1 ± 2.5 μm (40 measurements), which is larger than the size of the nucleus of HEK cells (12.5 ± 2.4 μm). Note that the measurement of the MT-1 nucleus size is based on nuclei within the cells; however, measurements on the unsuccessfully isolated MT-1 nuclei appear to give similar estimates. Furthermore, the same methodology applied to HEK cells produced almost identical distributions for the sizes of the *in situ* and isolated nuclei. The measured differential in integrated backscatter coefficient also may be due to differences in density and compressibility between cells (Shung et al. 1993), as well as scatterer randomization (Hunt et al. 2002). However, because the values of speed of sound are similar for all cells and the attenuation is similar, large differences are not anticipated in density and compressibility between cell types. Scatterer randomization is difficult to ascertain, as the nature of the scatterer is unknown; however, large deviations in this parameter again are not expected. Therefore, the variation in effective scatterer size is a reasonable explanation for the backscatter differences.

The ultrasound wavelength, λ, at 40 MHz is approximately 38 μm, the same order of magnitude as the size of cells. This complicates the analysis, because most theory has been developed for the case when the scatterer (or effective scatterer) diameter is considerably smaller than λ. In the long-wavelength limit and for single-particle scattering, the integrated backscatter coefficient is expected to be proportional to the square of the particle volume (a^3). In these experiments, the backscatter coefficient increases as roughly proportionate to the fourth power of the diameter of the nucleus instead of the sixth power, as would be expected if the nucleus were the dominant scatterer and the scatterer diameter were not small compared with the wavelength. In the long-wavelength limit, backscatter intensity also depends on the fourth power of the frequency (f^4). Figure 11a shows backscatter coefficient as a function of frequency for

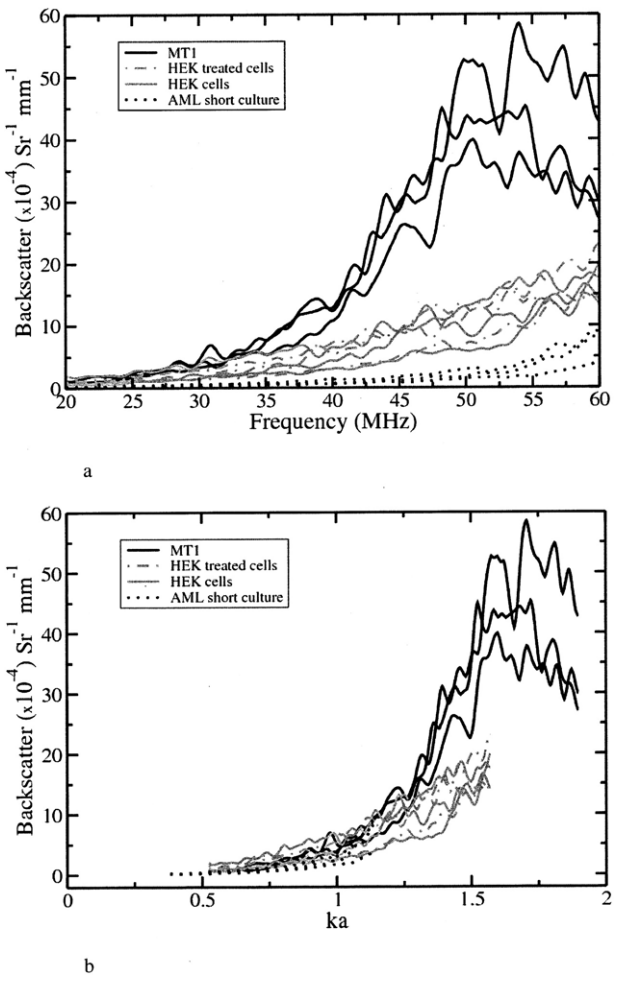

Fig. 11. (a) Backscatter as a function of frequency for cells used in the experiments (MT1–solid black, HEK treated–intermittent gray, HEK untreated–solid gray and AML short culture–dotted black). Three experiments were performed for each cell type. (b) The data from (a) replotted as a function of ka (wave number times scatterer radius), assuming a scatterer radius equal to the measured radius of the nucleus of the cell (MT1: 15.1 μm, HEK: 12.5 μm and AML short culture 9.1 μm).

four of the five cell lines used (for sake of clarity). The three curves for each cell type represent experiments done on different pellets. The trend toward higher backscatter coefficient at higher frequencies can be clearly seen, even although fits show f^3 relationships between backscatter and frequency for most cell lines. Interestingly, the backscatter decreases for the MT-1 cell line at frequencies above 50 MHz. Figure 11b replots the data of Fig. 11a as a function of ka (wavenumber times scatterer radius), assuming the nucleus to be the scatterer. Figure 11b shows that considerable overlap exists among the backscatter curves for most cell lines, which suggests that the nucleus may be contributing significantly to the backscatter. Similar decreases in backscatter at ka values above 1.5 have been shown by Anderson (1950) in his theoretical examination of scattering from low-contrast fluid spheres.

Few other studies have measured absolute integrated backscatter coefficient in tissues using high-frequency ultrasound. The majority report only relative values. Machado et al. (2002) reported a value of $4.26 \pm 2.34 \times 10^{-3}$ Sr^{-1} mm^{-1} for a foam cell layer in human coronary arteries using a 50 MHz transducer. Raju and Srinivasan (2001) found an integrated backscatter of 1.57 to 47.7×10^{-3} Sr^{-1} mm^{-1} for forearm dermis using a frequency range of 14 to 34 MHz. Our results of 1.71×10^{-4} to 26.47×10^{-4} Sr^{-1} mm^{-1} are within the range of those reported in the literature (Foster et al. 2000). Foam cells are approximately 20 μm in diameter (Hillman and Engelman 1976) and arise when monocytes differentiate into macrophages and accumulate lipids (Linton and Fazio 2003). A higher backscatter coefficient would be expected for foam cells than for those in our study because foam cells contain fat/nonfat interfaces that are known to increase backscatter. We would also expect our values to have a lower backscatter coefficient than skin, which has a high concentration of collagen. The compressibility and density of collagen are very different from other tissue components, which results in relatively stronger scattering for collagen entities.

In our experiments, cells were centrifuged to form a compact aggregate of cells and this aggregate was ultrasonically characterized. We have used the cell pellet system successfully in the past to image cells and the histology indicates that pellets consisted of a continuum of cellular material (Kolios et al. 2003; Tunis et al. 2005). From a modeling perspective, one could thus envision that the nuclei are suspended scatterers in a continuum of cytoplasm. This model is of particular interest to our group, as it emulates cell organization in tumors. In fact, recent experiments in our laboratory, as well as others (Oelze et al. 2005), indicate that cells in pellet form and solid tumors grown from the same cells injected subcutaneously in animals have very similar backscattering characteristics. However, to model this system fully, knowledge of properties such as the density and compressibility of the different types of cells and subcellular components is required. This knowledge might have allowed us to rigorously relate the measured ultrasonic properties to the physical properties of the cells and nuclei and thus to provide a better interpretation of our results. Experiments that are underway and planned use acoustic microscopy and microrheology techniques to measure directly and indirectly these acoustic properties and to obtain a better fundamental understanding of ultrasound scattering at these scales. This fundamental understanding will assist in relating ultrasonic parameters to physical tissue properties, a long time goal of the late Frederic Lizzi (Lizzi et al. 1983, 1988, 1996).

Acknowledgments—The authors acknowledge the generous support of the Whitaker Foundation (grants RG-01 to 0141) and the Natural Sciences and Engineering Research Council (NSERC, CHRP grant 237962 to 2000). The VisualSonics ultrasound imaging instrument was purchased with the financial support of the Canada Foundation for Innovation, the Ontario Innovation Trust and Ryerson University. The authors thank Arthur Worthington, Adam Tunis and Jill Tymchak for technical assistance, Jing Jin for providing HEK-293 cells and the handling expertise, Harold E. Frey for critical assistance in the nucleus isolation procedures and Michael D. Sherar for valuable discussions. LT also was supported through an Undergraduate Student Research Award from NSERC and a Harold E. Johns Summer Studentship Award.

REFERENCES

Anderson VC. Sound scattering from a fluid sphere. J Acoust Soc Am 1950;22:426–431.

Baddour RE, Sherar MD, Hunt JW, Czarnota GJ, Kolios MC. High-frequency ultrasound scattering from microspheres and single cells. J Acoust Soc Am 2005;117:934–943.

Bamber JC. Attenuation and absorption. In: Hill CR, Bamber JC, and ter Haar GR, eds. Physical principles of medical ultrasonics, second edition. Mississauga, Ontario, Canada: John Wiley & Sons Canada Ltd., 2004.

Bridal SL, Fornes P, Bruneval P, Berger G. Parametric (integrated backscatter and attenuation) images constructed using backscattered radio frequency signals (25–56 MHz) from human aortae *in vitro*. Ultrasound Med Biol 1997;23:215–29.

Cloutier G, Daronatand M, Savery D, et al. Non-Gaussian statistics and temporal variations of the ultrasound signal backscattered by blood at frequencies between 10 and 58 MHz. J Acoust Soc Am 2004; 116:566–577.

Costa KD. Single-cell elastography: Probing for disease with the atomic force microscope. Dis Markers 2003;19:139–154.

Czarnota GJ, Kolios MC, Vaziri H, et al. Ultrasonic biomicroscopy of viable, dead and apoptotic cells. Ultrasound Med Biol 1997;23: 961–965.

Czarnota GJ, Kolios MC, Abraham J, et al. Ultrasound imaging of apoptosis: High-resolution non-invasive monitoring of programmed cell death *in vitro*, *in situ* and *in vivo*. Br J Cancer 1999;81:520–527.

Czarnota GJ, Kolios MC, Hunt JW, Sherar MD. Ultrasound imaging of apoptosis. DNA-damage effects visualized. Methods Mol Biol 2002;203:257–277.

D'Astous FT, Foster FS. Frequency dependence of ultrasound attenuation and backscatter in breast tissue. Ultrasound Med Biol 1986; 12:795–808.

Dent C L, Scott MJ, Wickline SA, Hall CS. High-frequency ultrasound for quantitative characterization of myocardial edema. Ultrasound Med Biol 2000;26:375–384.

Duck FA. Physical properties of tissue: A comprehensive reference book. London: Academic Press, 1990.

Forsberg F. Ultrasonic biomedical technology; marketing versus clinical reality. Ultrasonics 2003;42:17–27.

Foster FS, Pavlin CJ, Harasiewicz KA, Christopher DA, Turnbull DH. Advances in ultrasound biomicroscopy. Ultrasound Med Biol 2000; 26:1–27.

Hengartner MO. The biochemistry of apoptosis. Nature 2000;407:770–776.

Hillman GM, Engelman DM. Compositional mapping of cholesteryl ester droplets in the fatty streaks of human aorta. J Clin Invest 1976;58:1008–1018.

Hunt JW, Worthington AE, Xuan A, et al. A model based upon pseudo regular spacing of cells combined with the randomisation of the nuclei can explain the significant changes in high-frequency ultrasound signals during apoptosis. Ultrasound Med Biol 2002;28:217–226.

Jin J, Woodgett JR. Chronic activation of protein kinase Bbeta/Akt2 leads to multinucleation and cell fusion in human epithelial kidney cells: events associated with tumorigenesis. Oncogene 2005;24(35): 5459–5470.

Kolios MC, Czarnota GJ, Lee M, Hunt JW, Sherar MD. Ultrasonic spectral parameter characterization of apoptosis. Ultrasound Med Biol 2002;28:589–597.

Kolios MC, Taggart L, Baddour RE, et al. An investigation of backscatter power spectra from cells, cell pellets and microspheres. Ultrasonics Sympos IEEE 2003:752–757.

Kolios MC, Czarnota GJ, Worthington AE, Giles A, Sherar MD. Towards understanding the nature of high frequency ultrasound backscatter from cells and tissues: An investigation of backscatter power spectra from different concentrations of cells of different sizes. IEEE International Ultrasonics, Ferroelectrics, and Frequency Control 50th Anniversary Joint Conference, Montreal, Canada 2004:606–609.

Liang HD, Blomley MJ. The role of ultrasound in molecular imaging. Br J Radiol 2003;76 (Spec No 2):S140–S150.

Linton MF, Fazio S. Macrophages, inflammation and atherosclerosis. Int J Obes Relat Metab Disord 2003;27 (Suppl 3):S35–S40.

Lizzi FL, Greenebaum M, Feleppa E J, Elbaum M, Coleman DJ. Theoretical framework for spectrum analysis in ultrasonic tissue characterization. J Acoust Soc Am 1983;73:1366–1373.

Lizzi FL, King DL, Rorke MC, et al. Comparison of theoretical scattering results and ultrasonic data from clinical liver examinations. Ultrasound Med Biol 1988;14:377–385.

Lizzi FL, Astor M, Kalisz A, et al. Ultrasonic spectrum analysis for assays of different scatterer morphologies: Theory and very-high frequency clinical results. Proceedings of the 1996 IEEE Ultrasonics Symposium. Part 2 (of 2), Nov, 1996, 1155–1159. San Antonio, TX, USA: IEEE, Piscataway, NJ, USA.

Lupotti FA, Zimmer A, Daronat M, et al. Effects of aggregation of red cells and linear velocity gradients on the correlation-based method for quantitative IVUS blood flow at 20 MHz. Ultrasound Med Biol 2004;30:205–214.

Machado JC, Foster FS, Gotlieb AI. Measurement of the ultrasonic properties of human coronary arteries *in vitro* with a 50-MHz acoustic microscope. Braz J Med Biol Res 2002;35:895–903.

Meselson M, Stahl FW. The replication of DNA in Escherichia-coli. Proc Natl Acad Sci U S A 1958;44:671–682.

Muramatsu M, Hayashi Y, Onishi T, Sakai M, Takai, K. Rapid isolation of nucleoli from detergent purified nuclei of various tumor and tissue culture cells. Exp Cell Res 1974;88:245–251.

Muramatsu M, Onishi T. Rapid isolation of nucleoli from detergent-purified nuclei of tumor and tissue culture cells. Methods Cell Biol 1977;15:221–234.

Nguyen CT, Hall CS, Scott MJ, et al. Age-related alterations of cardiac tissue microstructure and material properties in Fischer 344 rats. Ultrasound Med Biol 2001; 27:611–619.

Oelze ML, O'Brien WD, Jr., Blue JP, Zachary JF. Differentiation and characterization of rat mammary fibroadenomas and 4T1 mouse carcinomas using quantitative ultrasound imaging. IEEE Trans Med Imaging 2004;23:764–771.

Oelze ML, O'Brien WD, Zachary JF. High frequency quantitative ultrasound imaging of solid tumors in mice. Proceedings of the 28th International Acoustical Imaging Symposium. San Diego, CA, 2005, In press.

Pavlin CJ, Harasiewicz K, Sherar MD, Foster FS. Clinical use of ultrasound biomicroscopy. Ophthalmology 1991;98(3):287–295.

Raju BI, Srinivasan MA. High-frequency ultrasonic attenuation and backscatter coefficients of *in vivo* normal human dermis and subcutaneous fat. Ultrasound Med Biol 2001;27:1543–1556.

Saijo Y, Tanaka M, Okawai H, et al. Ultrasonic tissue characterization of infarcted myocardium by scanning acoustic microscopy. Ultrasound Med Biol 1997;23: 77–85.

Sarvazyan AP, Hill CR. Physical chemistry of the ultrasound-tissue interaction, physical principles of medical ultrasonics. 2nd ed. Hill CR, Bamber JC, G. R. ter Haar, GR, eds. John Wiley and Sons, 2004.

Shung KK, Thieme GA. Ultrasonic scattering in biological tissues. Boca Raton: CRC Press, 1993.

Tseng Y, Lee JS, Kole TP, Jiang I, Wirtz D. Micro-organization and

visco-elasticity of the interphase nucleus revealed by particle nanotracking. J Cell Sci 2004;117: 2159–2167.

Tunis AS, Spurrell D, McAlduff D, et al. High frequency ultrasound signal statistics from mouse mammary tissue during involution. Proceedings of the IEEE International Ultrasonics, Ferroelectrics, and Frequency Control 50th Anniversary Joint Conference, Montreal, Canada, 2004:768–771.

Tunis AS, Czarnota GJ, Giles A, et al. Monitoring structural changes in cells with high frequency ultrasound signal statistics. Ultrasound Med Biol 2005;31: 1041–1049.

Turnbull DH, Wilson SR, Hine AL, Foster FS. Ultrasonic characterization of selected renal tissues. Ultrasound Med Biol 1989;15: 241–253.

Ursea R, Coleman DJ, Silverman RH, et al. Correlation of high-frequency ultrasound backscatter with tumor microstructure in iris melanoma. Ophthalmology 1998;105(5):906–912.

Vlad RM, Czarnota GJ, Giles A, et al. High-frequency ultrasound for monitoring changes in liver tissue during preservation. Phys Med Biol 2005;50:197–213.

Wang C, Koistinen P, Yang GS, et al. Mast cell growth factor, a ligand for the receptor encoded by c-kit, affects the growth in culture of the blast cells of acute myeloblastic leukemia. Leukemia 1991;5: 493–499.

Worthington AE, Sherar MD. Changes in ultrasound properties of porcine kidney tissue during heating. Ultrasound Med Biol 2001 27, 673–682.